BMP signaling controls buckling forces to modulate looping morphogenesis of the gut

Nandan L. Nerurkar[a], L. Mahadevan[b,c,d,e,f,1], and Clifford J. Tabin[a,1]

[a]Department of Genetics, Harvard Medical School, Boston, MA 02115; [b]School of Engineering and Applied Sciences, Harvard University, Cambridge, MA 02138; [c]Department of Organismic and Evolutionary Biology, Harvard University, Cambridge, MA 02138; [d]Department of Physics, Harvard University, Cambridge, MA 02138; [e]Wyss Institute for Biologically Inspired Engineering, Harvard University, Cambridge, MA 02138; and [f]Kavli Institute for Bionano Science and Technology, Harvard University, Cambridge, MA 02138

Contributed by Clifford J. Tabin, January 16, 2017 (sent for review September 26, 2016; reviewed by Lance Davidson and Natasza Kurpios)

Looping of the initially straight embryonic gut tube is an essential aspect of intestinal morphogenesis, permitting proper placement of the lengthy small intestine within the confines of the body cavity. The formation of intestinal loops is highly stereotyped within a given species and results from differential-growth–driven mechanical buckling of the gut tube as it elongates against the constraint of a thin, elastic membranous tissue, the dorsal mesentery. Although the physics of this process has been studied, the underlying biology has not. Here, we show that BMP signaling plays a critical role in looping morphogenesis of the avian small intestine. We first exploited differences between chicken and zebra finch gut morphology to identify the BMP pathway as a promising candidate to regulate differential growth in the gut. Next, focusing on the developing chick small intestine, we determined that *Bmp2* expressed in the dorsal mesentery establishes differential elongation rates between the gut tube and mesentery, thereby regulating the compressive forces that buckle the gut tube into loops. Consequently, the number and tightness of loops in the chick small intestine can be increased or decreased directly by modulation of BMP activity in the small intestine. In addition to providing insight into the molecular mechanisms underlying intestinal development, our findings provide an example of how biochemical signals act on tissue-level mechanics to drive organogenesis, and suggest a possible mechanism by which they can be modulated to achieve distinct morphologies through evolution.

intestinal looping | buckling | biomechanics | Bmp | morphogenesis

Differential growth represents one of the core physical mechanisms driving morphogenesis throughout the vertebrate embryo (1–9). Investigations into the mechanics of differential growth have often illustrated key physical parameters (e.g., tissue stiffness, growth rates, and initial geometry) that determine the resultant tissue shape. Ultimately, however, these parameters must be under genetic control. However, at present, there are only a limited few examples of how developmental signals are integrated with downstream physical properties to shape the embryo. Here, we build on our detailed understanding of the physics of loop morphogenesis in the chick small intestine (1) to ask what molecular cues underlie this important physical transformation during gastrointestinal development.

Looping maximizes the absorptive capacity of the gut by allowing intestinal length to extend well beyond the linear length of the organism, while maintaining an ordered configuration in the body cavity. Errors in looping, such as malrotation of the gut, can result in obstruction of the bowel or strangulation of the abdominal circulation, a condition known as midgut volvulus (10). Among birth defects, intestinal malrotation is relatively common in newborns and can be fatal if left untreated (11, 12). Early during looping morphogenesis, the initially straight midgut forms a primary loop that extends into the yolk stalk (umbilicus in mammals). Subsequent loops continue to form outside the body cavity as the midgut elongates, until the looped intestine retracts into the body cavity before birth. Although the intestine continues to elongate, no further loops form after birth. The number and shape of intestinal loops are remarkably conserved within a given species (1, 10). In previous work, we demonstrated that this precisely stereotyped looping results from physical forces that arise due to elongation of the initially straight gut tube against the constraint of the dorsal mesentery, a thin membranous tissue that anchors the gut tube to the body wall (1). As the gut tube elongates, it stretches the mesentery, which in turn compresses the tube. As a result of these compressive forces, the gut tube buckles into a looped configuration. The curvature and wavelength of loops can be mathematically predicted from experimentally measured parameters describing geometry and stiffness of the tube and mesentery, and differential elongation between the two tissues (1). Equipped with an understanding of the physics involved, here we aim to elucidate the underlying signaling pathways that control intestinal looping in the chicken embryo.

Results

BMP Signaling Is Enriched in the Looping Chick Dorsal Mesentery. To identify pathways that may play role in looping morphogenesis, we exploited differences in how loops form between the developing chick and zebra finch embryo. Although, in both, looping results from differential growth between the gut tube and mesentery, the degree of differential growth is twofold higher in the chick than the finch (1). Because bone morphogenetic proteins (BMPs) have been strongly implicated in other aspects of gut and mesentery organogenesis (13–18), we compared BMP signaling in the embryonic chick and finch dorsal mesentery by immunofluorescent detection of phosphorylated Smad 1/5/8. In the chick, phospho-Smad levels temporally correlated with the progression of looping morphogenesis (Fig. 1*A* and Fig. S1*A*). Staining was detected at

Significance

During embryogenesis, the dramatic transformation from a seemingly disorganized mass of cells into the fully patterned adult form necessitates stereotyped regulation of forces at the genetic and molecular level. Although great progress has been made in understanding how gene expression and signaling generate biological pattern, little is known about how molecular cues organize forces to sculpt physical patterns during development. The present work identifies BMP signaling as a key pathway in controlling looping of the small intestine, a process driven by mechanical buckling due to elongation of the intestine against the constraint of a neighboring tissue, the dorsal mesentery.

Author contributions: N.L.N., L.M., and C.J.T. designed research; N.L.N. performed research; N.L.N., L.M., and C.J.T. analyzed data; and N.L.N., L.M., and C.J.T. wrote the paper.

Reviewers: L.D., University of Pittsburgh; and N.K., Cornell University.

The authors declare no conflict of interest.

[1]To whom correspondence may be addressed. Email: tabin@genetics.med.harvard.edu or lm@seas.harvard.edu.

This article contains supporting information online at www.pnas.org/lookup/suppl/doi:10.1073/pnas.1700307114/-/DCSupplemental.

low levels at the start of looping at embryonic day 10 (E10), increased markedly by E12 when looping is underway, and remained elevated through the completion of looping at E16 (Fig. 1*A* and Fig. S1*A*). Compared with the chick, phospho-Smad levels in the finch dorsal mesentery remained relatively low throughout looping, which occurs between E9 and E11 (Fig. 1*B*). In the gut tube, however, where BMP is signaling is indispensable for radial patterning (13, 17, 18), phospho-Smad staining was similarly high in both the chick and finch, indicating that antibody reactivity was similar in both species. Therefore, BMP signaling correlates with differential growth across species and, in the chick, correlates temporally with the progression of looping morphogenesis. To examine the pathway more closely, we next observed the expression of BMP ligands and receptors in the chick. During looping, *Bmp2* was highly expressed within the dorsal mesentery and was dorsally biased within the gut tube itself (Fig. 2*A* and Fig. S1*B*). On the other hand, Bmps 4 and 7 were expressed symmetrically within the gut tube and undetected in the mesentery (Fig. 2 *B* and *C*, and Fig. S1*F*). Therefore, although *Bmp 4* and *7* are expressed in a pattern consistent with a role in radial patterning of the gut tube, *Bmp2* is not. BMP receptors were also strongly expressed throughout the dorsal mesentery and gut tube (Fig. S1 *C–E*). These results suggest a possible role for *Bmp2* in looping morphogenesis.

BMP Activity Directly Modulates Loop Morphology. To functionally test the role of BMP signaling in looping morphogenesis, we developed a method to infect the chick midgut with the replication-competent retrovirus RCAS (Fig. S2 *A–C*), and then used this approach to either activate or inhibit BMP signaling using RCAS-Bmp2 and RCAS-Noggin viruses, respectively (Fig. S2*D*).

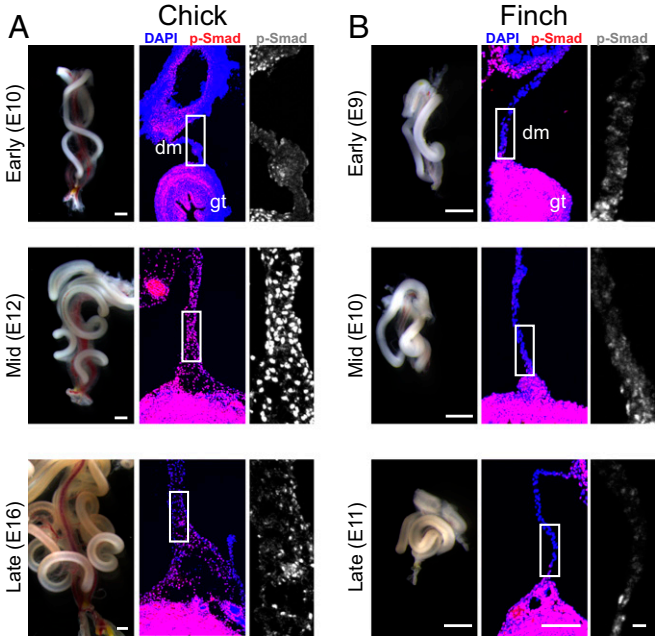

Fig. 1. BMP activity in the dorsal mesentery correlates with differential growth across development and between species. (*A*) Phospho-Smad 1/5/8 staining in the chick dorsal mesentery at early (E10) to mid (E12) and late (E16) looping stages. (*B*) Phospho-Smad 1/5/8 staining in the zebra finch dorsal mesentery at early (E9) to mid (E10) and late (E11) looping stages. All sections are from the distal jejunum and proximal ileum. For each, whole-mount bright field of the intestine is shown at *Left* (scale bar: 1 mm); immunofluorescent staining for phospho-Smad (red) and DAPI counterstain (blue) is shown at *Center* (scale bar: 100 μm), and the boxed region indicates the isolated phospho-Smad signal magnified at *Right* (scale bar: 10 μm). dm, dorsal mesentery; gt, gut tube.

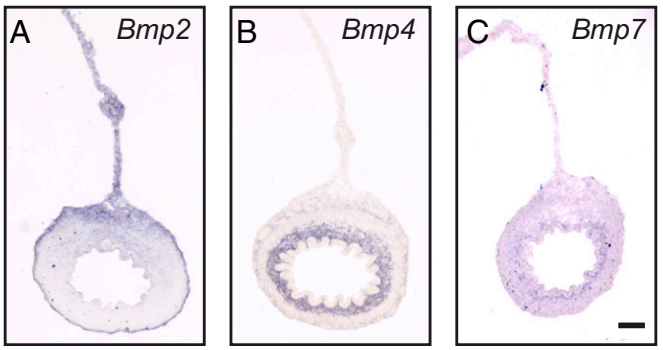

Fig. 2. BMP ligand and receptor expression during looping of the small intestine. In situ hybridization of the E12 chick small intestine for expression of BMP ligands *Bmp2* (*A*), *Bmp4* (*B*), and *Bmp7* (*C*) on sections from the distal jejunum and proximal ileum. (Scale bar: 100 μm.)

The timing of injection (E5) permitted normal radial patterning of gut smooth muscle (Fig. S2*E*), a BMP-dependent process (13, 17, 18) that completes shortly after looping begins. Infection of the gut with RCAS-Bmp2 resulted in more tightly coiled loops than RCAS-GFP, whereas RCAS-Noggin infection resulted in dramatically reduced coiling in the intestine (Fig. 3 *A–F*). Quantification of loop morphology revealed a significant increase in loop number with RCAS-Bmp2 infection (Fig. 3*G*), along with a significant decrease in wavelength λ (length of tube per loop, Fig. 3*H*), and radius of curvature R (Fig. 3*I*). Conversely, RCAS-Noggin significantly reduced the number of loops formed, and loops were characterized by a larger wavelength and radius of curvature (Fig. 3 *G–I*). Therefore, both gain- and loss-of-function experiments strongly implicate BMP signaling in controlling looping morphogenesis of the small intestine.

BMP Signaling Negatively Regulates Elongation of the Mesentery. Wild-type loop morphology is a function of geometric, elastic, and growth properties of the gut tube and mesentery. We next focused on identifying specifically which of these properties BMP acts on to determine looping morphology. Because differential growth between the gut tube and mesentery provides the driving force for looping, we first determined how modulation of BMP activity alters differential growth. To do so, the gut tube was dissected away from the mesentery to relieve forces due to differential growth, and the length of the separated mesentery (L_m) and gut tube (L_t) were measured. Size of the dorsal mesentery was significantly reduced following RCAS-Bmp2 infection and increased with RCAS-Noggin (Fig. 4 *A–D*). For both, however, gut tube length was unaffected (Fig. 4*E*). The length mismatch between the tube and mesentery indicates the extent of differential growth between these tissues, quantified as the differential growth strain $\varepsilon_p = (L_t/L_m) - 1$. ε_p was significantly increased with RCAS-Bmp2, and decreased with RCAS-Noggin (Fig. 4*F*). In other words, activation of the pathway accentuates differential growth—and as a result, compressive buckling forces—by suppressing elongation of the mesentery, whereas inhibition of the pathway decreases differential growth due to increased elongation of the mesentery. In addition to increasing mesentery length, RCAS-Noggin caused an increase tube radius and mesentery thickness (Fig. 4*G*).

To understand how BMP negatively regulates mesenteric growth, we next examined cell density in the dorsal mesentery. Surprisingly, cell density varied directly with BMP activity: RCAS-Bmp2 infection significantly increased cell density, whereas RCAS-Noggin caused a significant reduction (Fig. 4 *H–K*). Although in RCAS-GFP– and RCAS-Bmp2–infected mesenteries, the cellular morphology was spindle-like and irregular

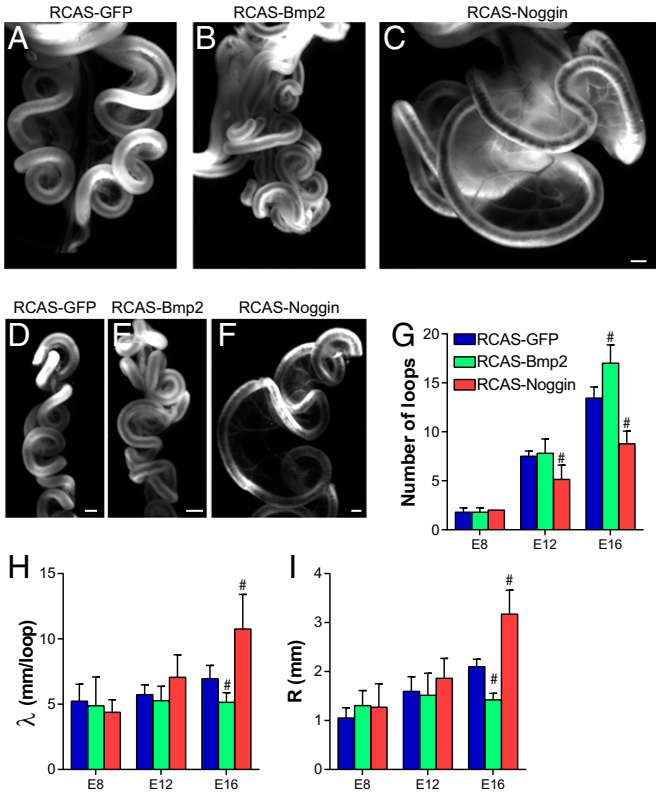

Fig. 3. BMP activity modulates looping morphogenesis of the small intestine. (*A–C*) Whole-mount bright-field images of E16 chick intestines following infection at E5 with RCAS-GFP (*A*), RCAS-Bmp2 (*B*), and RCAS-Noggin (*C*). (Scale bar: 1 mm.) (*D–F*) Right lateral views of the dissected E16 chick intestines following removal of the superior mesenteric artery from the mesentery for RCAS-GFP (*D*), RCAS-Bmp2 (*E*), and RCAS-Noggin (*F*)–infected intestines; intestines are oriented from top/proximal to bottom/distal in each panel. (Scale bar: 1 mm.) (*G–I*) Quantification of loop number (*G*), wavelength λ (*H*), and radius of curvature *R* (*I*) of intestinal loops over developmental stage following infection with RCAS-GFP, RCAS-Bmp2, and RCAS-Noggin at E5. $n = 5–9$ per condition. $^{\#}P \leq 0.05$ compared with RCAS-GFP at the equivalent developmental stage.

(Fig. 4 *H* and *I*), inhibition of BMP activity with RCAS-Noggin resulted in large cuboidal cells with dense cortically enriched F-actin (Fig. 4*J*). Finally, we measured tissue volume in the gut tube and mesentery. Compared with RCAS-GFP, Bmp2 overexpression had no effect on gut tube volume but caused a significant decrease in dorsal mesentery volume (Fig. 4*L*). RCAS-Noggin caused a significant increase in both tube and mesentery volume. Therefore, in the dorsal mesentery, cell density varies directly with BMP activity, whereas tissue volume varies inversely. Strikingly, these measurements suggest that the total cell number in the dorsal mesentery (cell density × tissue volume) is nearly identical for RCAS-GFP, RCAS-Bmp2, and RCAS-Noggin infected embryos, despite clear differences in tissue size.

Tensile Modulus of the Gut Tube and Mesentery Are Unaltered by BMP Signaling. Although differential growth between the gut tube and mesentery provides the buckling forces necessary for looping, the resulting loop morphology also depends on the geometry and stiffness (modulus) of these two tissues (1). Therefore, to fully understand the key biomechanical properties BMP signaling acts on during looping, it is necessary to determine how Bmp2 and Noggin affect tube and mesentery modulus. Tensile testing of the gut tube following infection with RCAS-Bmp2 and RCAS-Noggin showed no change in tensile modulus compared with RCAS-GFP (Fig. 5 *A* and *D*, and Fig. S3 *A–C*). As described previously (1), the dorsal mesentery has a nonlinear stress–strain behavior characteristic of many biological soft tissues (19, 20). This means that, as the tissue is stretched, it is initially soft (low modulus) but at higher strains the tissue stiffens and the modulus becomes constant (Fig. 5*B*). Although stress–strain nonlinearity of the dorsal mesentery was observed in each condition, the degree to which the mesentery can be stretched before stiffening (the transition strain ε^*, Fig. S3*C*) was significantly reduced following RCAS-Noggin infection (Fig. 5 *B* and *C*). Nonetheless, the linear modulus (slope of the stress–strain curve at high stretch; Fig. S3*C*) was identical for RCAS-GFP–, RCAS-Bmp2–, and RCAS-Noggin–infected dorsal mesenteries (Fig. 5*D*). In other words, the extent to which the mesentery stretches before significantly resisting further deformation is reduced with RCAS-Noggin, but once it does stiffen, resistance to further stretching is identical to RCAS-GFP and RCAS-Bmp2.

Scaling Laws Reveal the Biomechanical Targets of BMP Signaling That Determine Loop Morphology. In previous work, we derived simple scaling laws to relate a handful of experimentally measured properties of the developing wild-type gut to the resulting morphology of loops (1). Here, we revisited these scaling relationships to dissect the morphological phenotypes associated with BMP activation and inhibition. As described previously, minimizing the sum of strain energies associated with stretching of the mesentery and bending of the gut tube yields a scaling relation for looping wavelength λ of the form (1): $\lambda \propto (E_t I_t / E_m h)^{1/3}$, where $E_{t/m}$ is the tube/mesentery modulus, $I_t \propto (r_o^4 - r_i^4)$ is the moment of inertia of the tube, $r_{o/i}$ is the outer/inner radius of the gut tube, and h is the mesentery thickness. Similarly, a scaling law for the radius of curvature R is obtained from a torque balance between the tube and mesentery (1): $R \propto (E_t I_t / E_m h \varepsilon_o^2)^{1/3}$, where ε_o is the effective differential growth strain, defined as the growth strain beyond ε^* (1). Therefore, the scaling laws allow for the loop morphology, quantified as λ (Fig. 3*H*) and *R* (Fig. 3*I*), to be predicted from six parameters, each of which we have measured experimentally following misexpression of Bmp2 and Noggin (Figs. 4 *F* and *G*, and 5*D*). We first used the results for RCAS-GFP to determine the constant of proportionality for these scaling laws, and then used this to predict loop morphology for both RCAS-Bmp2 and RCAS-Noggin phenotypes. Using no free parameters, the scaling laws successfully predicted both the λ (Fig. 5*E*) and *R* (Fig. 5*F*) for Bmp2 and Noggin phenotypes. Next, we calculated the extent to which each of the measured changes contributes to the looping phenotype compared with RCAS-GFP (Fig. 5*G*). Changes in tube radius accounted for the majority of the observed changes in λ for both RCAS-Bmp2, which decreased λ, and RCAS-Noggin, which increased λ. The tight coils (decreased *R*) of the RCAS-Bmp2 phenotype were predominantly the result of an increase in differential growth, due to a reduction in the elongation rate of the dorsal mesentery. On the other hand, the looser loops (higher *R*) of the RCAS-Noggin phenotypes were predominantly due to equal contributions from an increase in tube radius and a decrease in differential growth.

BMP Signaling Required for Internalization of the Small Intestine. The intestine normally loops outside the embryo and is then internalized into the body cavity before birth. Because RCAS-Noggin infection resulted in intestines with large and irregular loops, we asked whether internalization of the gut is also affected. At E20 (1 d before hatching), only the membranes of the yolk stalk protruded from the ventral body wall of RCAS-GFP–infected embryos (Fig. S4). However, in RCAS-Noggin–infected embryos, the entire small intestine remained outside the body cavity (Fig. S4). The phenotype closely resembles gastroschisis, a congenital disorder in which babies are born with their intestines protruding from a hole in the ventral body wall (10). It is important to note, however, that by E20, it is likely that the virus has spread throughout the embryo, including the ventral body wall. As

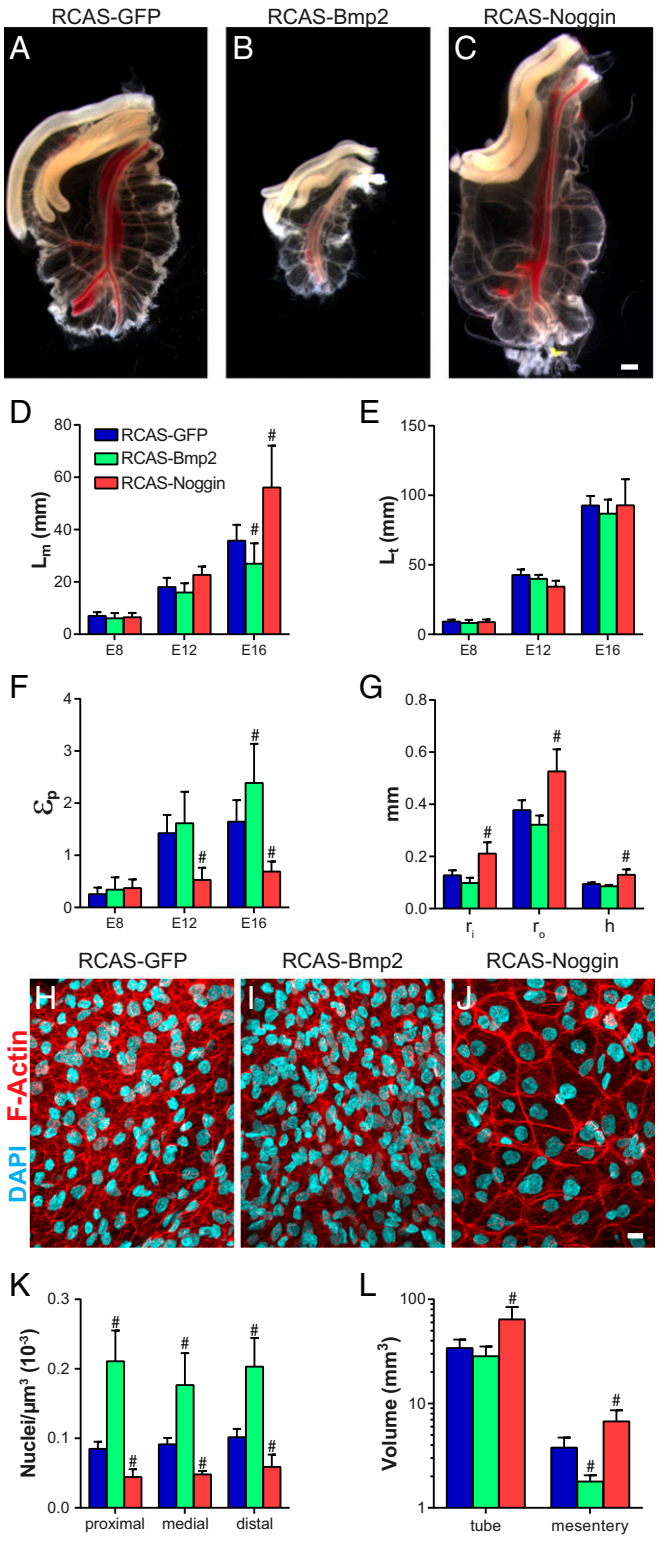

Fig. 4. BMP activity controls differential growth between the gut tube and mesentery. (*A–C*) Whole-mount bright-field images of dorsal mesentery following dissection to remove gut tube from E16 embryos following infection with RCAS-GFP (*A*), RCAS-Bmp2 (*B*), and RCAS-Noggin (*C*). (Scale bar: 1 mm.) (*D–F*) Quantification of dorsal mesentery length L_m (*D*), gut tube length L_t (*E*), and physiological growth strain ε_p (*F*) over developmental stage following infection with RCAS-GFP, RCAS-Bmp2, and RCAS-Noggin at E5. (*G*) Gut tube inner (r_i) and outer (r_o) radii and mesentery thickness (h), measured at E16 following infection with RCAS-GFP, RCAS-Bmp2, and RCAS-Noggin. n = 5–9 per condition. $^{\#}P \leq 0.05$ compared with RCAS-GFP at the equivalent developmental stage. (*H–J*) DAPI- and phalloidin-stained whole mounts of dorsal mesentery at E16 following infection with RCAS-GFP (*H*), RCAS-Bmp2 (*I*), and RCAS-Noggin (*J*). (Scale bar: 10 μm.) (*K* and *L*) Cell density (*K*) (n = 3 embryos) in the proximal, medial, and distal jejunal dorsal mesentery, and total dorsal mesentery volume (*L*) (n = 5–6) at E16. $^{\#}P \leq 0.05$ compared with RCAS-GFP at the equivalent location (*K*) or tissue (*L*).

such, it is unclear to what extent Noggin-induced gastroschisis is related to the looping phenotype. Nonetheless, these findings implicate BMP signaling in proper internalization of the intestine before birth, supporting previous observations in the mouse (21).

Discussion

Absorption of nutrients in the small intestine is optimized by two important morphological adaptations: villi, which maximize surface area within the radial constraints of the intestinal tube, and looping, which maximizes intestinal length within the spatial constraints of the body cavity. Although recent work has identified developmental signals involved in villus formation (15, 22, 23), the molecular mechanisms underlying looping of the intestine have remained largely unknown. On the other hand, the physics of intestinal looping has been well characterized (1). The present work builds on this by implicating the molecular signal Bmp2 in the process, and quantitatively identifies the biomechanical parameters BMPs act on to control looping morphogenesis. Looping results from compressive forces generated by differential growth between the rapidly elongating gut tube and its attached mesentery, which elongates much slower. Our findings suggest that this growth mismatch between the two tissues is due in part to *Bmp2*, which acts to suppress elongation of the dorsal mesentery. Accordingly, when *Bmp2* expression is increased by retroviral misexpression, elongation of the mesentery is reduced while tube elongation is unaffected, accentuating the growth disparity between these two tissues. Consequently, the mesentery applies larger compressive forces to the gut tube, resulting in an increase in the number and curvature of intestinal loops as it buckles. Conversely, inhibition by misexpression of the BMP antagonist *Noggin* resulted in a significant increase in mesentery perimeter, diminishing the growth disparity to produce fewer, straighter loops. In addition to shedding light on an important, yet poorly understood aspect of gastrointestinal development, this work illustrates how regulation of tissue-scale physical forces can be traced to signaling pathways during vertebrate development.

The Biomechanical Basis of BMP-Mediated Intestinal Looping. Upon identification of the BMP pathway as a modulator of loop morphology in the developing intestine, we performed a series of mechanical and morphological measurements to determine the how BMP signaling acts on physical properties to control this process. Our analysis suggests that, although BMP signaling may perform many functions during intestinal development, its role in looping morphogenesis can be almost entirely captured by how BMPs modulate just two geometric properties: tube radius and differential growth strain. For example, mesentery tension ($E_m h \varepsilon_o$), which provides the buckling forces that drive looping, was 2.5-fold higher following RCAS-Bmp2 infection. This was entirely the result of an increase in differential growth. Although we show at the tissue level that Bmp2 negatively regulates mesentery elongation, the associated cellular mechanism remains unclear. Surprisingly, we found that BMP activity had no effect on the total number of cells in the mesentery, despite dramatic changes in overall tissue volume. This eliminates BMP-mediated control of cell proliferation as a potential cellular mechanism. BMP inhibition caused a marked increase in cell size and restructuring of the actin cytoskeleton, suggesting that the regulation of cell size by BMP may contribute to the control of macroscopic tissue growth. This is but one possible

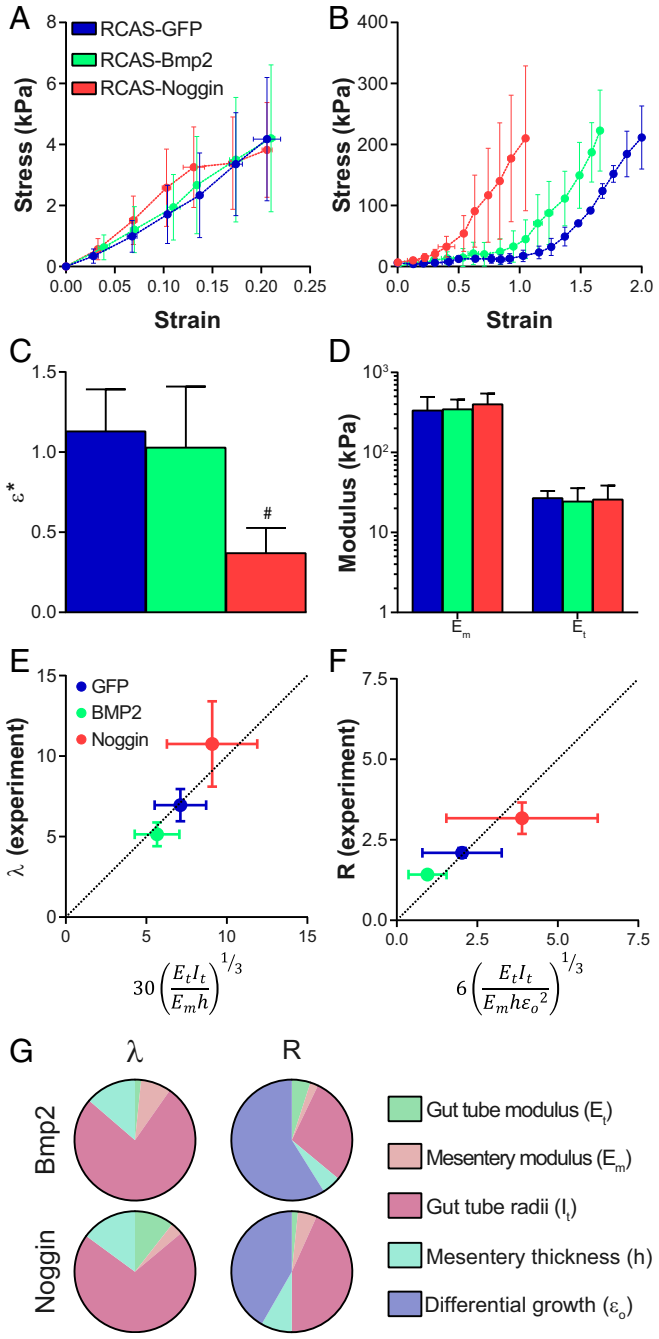

Fig. 5. BMP signaling acts on differential growth and intestinal diameter to determine loop morphology. Stress–strain curves from uniaxial tensile testing of gut tube (*A*) and dorsal mesentery (*B*) of E16 chicken embryos following infection with RCAS-GFP, RCAS-Bmp2, and RCAS-Noggin. (*C*) Transition strain ε^* from uniaxial tensile testing of E16 dorsal mesentery. $^{\#}P \leq 0.05$ compared with RCAS-GFP. (*D*) Tensile modulus of E16 dorsal mesentery (E_m) and gut tube (E_t). $n = 5$ per condition. (*E* and *F*) Comparison of experimentally measured (*y* axis) loop wavelength λ (*E*) and radius of curvature *R* (*F*) with scaling law predictions (*x* axis) for RCAS-GFP–, RCAS-Bmp2–, and RCAS-Noggin–infected E16 guts. (*G*) Contribution of each property in the scaling law to the predicted loop morphology for RCAS-Bmp2 and RCAS-Noggin.

mechanism of growth control, as cellular reorganization (e.g., convergent extension) and ECM deposition may also contribute to mesentery elongation. A potential role for BMP signaling in modulation of ECM production is supported by the observation that *Noggin* misexpression significantly reduced the transition strain ε^* (Fig. 5 *B* and *C*). This is indicative of changes in mesentery composition and structure (including for example the elastic fibers that appear in the dorsal mesentery at the onset of looping; Fig. S3*D*). A second intriguing possibility is that extensibility of the dorsal mesentery is itself regulated by stretch, and a loss of extensibility in RCAS-Noggin–infected embryos is secondary to a loss of stretch from diminished differential growth. There is growing evidence that tension in embryonic tissues can stimulate proliferation (24) and extracellular matrix production (25, 26), orient cell divisions (27, 28), drive gene expression (29, 30), and alter cell morphology (31, 32) and migration (33). It is unclear whether such mechanisms are at work in the developing gut. An interesting, albeit at this point speculative, possibility is that the signals controlling growth of the mesentery are themselves under control of physical forces, creating a feedback loop. There is evidence in other systems that *Bmp2* expression can be modulated by tension (34–36).

It is interesting to note that inhibition of BMPs in the gut tube by RCAS-Noggin caused a significant increase in tube radius (Fig. 4*G*) without altering tube length (Fig. 4*E*). This suggests that axial and radial growth of the gut are under control of distinct molecular signals. This is supported by a dramatic reduction in the intestinal length of *Fgf9*$^{-/-}$ and *Wnt5a*$^{-/-}$ mice, despite only minor changes in the radius (37, 38). From an evolutionary standpoint, it is sensible for selective pressure to decouple axial and radial growth of the gut tube: isotropic growth would produce guts that were not only longer, but thicker, and therefore with a larger bending stiffness. Consequently, although the need to produce more, tighter loops would be greater, the elastic energy required to form those loops would be as well. Instead, our results show that radial growth of the tube is controlled by the same molecular signal as mesentery length. For selective pressure to couple these two traits under the same genetic control makes sense, as increasing tube diameter and mesentery length would each diminish looping, whereas reducing tube diameter and mesentery length would each contribute to more and tighter loops.

Qualitatively, the reduced looping phenotype of RCAS-Noggin–infected embryos mirrors the loop morphology of the finch, whereas the increased looping phenotype with RCAS-Bmp2 resembles the mouse (1). Quantitatively, the effective differential growth strain ε_o (the amount by which the mesentery is stretched beyond its point of stiffening) is identical between RCAS-Noggin chicken embryos and the finch ($\varepsilon_o = 0.3$ for both). However, the loops of the RCAS-Noggin–infected chick are straighter than the finch ($R/r_o = 6$ vs. 2.7, respectively) due to the increased thickness (hence bending stiffness) of RCAS-Noggin–infected chick guts. On the other hand, ε_o was larger for RCAS-Bmp2–infected chick guts compared with the mouse ($\varepsilon_o = 1.3$ vs. 0.65, respectively), but associated with slightly straighter loops ($R/r_o = 4.4$ vs. 3.1, respectively) due, in part, to a higher stiffness contrast between mesentery and tube in the mouse. These comparisons highlight the important point that loop morphology depends not only on differential growth, but on geometry and stiffness of the tube and mesentery as well. Nonetheless, our findings that BMP activity correlate with differential growth of the gut and mesentery across species suggests one possible molecular mechanism by which evolutionary regulation of physical forces has created morphological diversity in the avian small intestine.

Materials and Methods

Experiments were conducted using fertilized eggs from White Leghorn chickens or zebra finches. Viral infections were conducted by injection of viral particles into the base of the yolk stalk at E5. Loop morphology was measured from dissected intestines following removal of superior mesenteric artery from the dorsal mesentery. Mechanical properties were measured by uniaxial tensile testing, using a linear actuator to apply tensile load at a slow, constant rate. Detailed protocols are provided in *SI Materials and Methods*.

ACKNOWLEDGMENTS. Finch eggs were kindly provided by Dr. Tim Gardner at Boston University. This work was supported by NIH Grants F32 HD069074 (to N.L.N.) and R01 HD087234 (to C.J.T.), and the MacArthur Foundation (to L.M.).

1. Savin T, et al. (2011) On the growth and form of the gut. *Nature* 476(7358):57–62.
2. Kim HY, et al. (2015) Localized smooth muscle differentiation is essential for epithelial bifurcation during branching morphogenesis of the mammalian lung. *Dev Cell* 34(6): 719–726.
3. Varner VD, Gleghorn JP, Miller E, Radisky DC, Nelson CM (2015) Mechanically patterning the embryonic airway epithelium. *Proc Natl Acad Sci USA* 112(30):9230–9235.
4. Oltean A, Huang J, Beebe DC, Taber LA (2016) Tissue growth constrained by extracellular matrix drives invagination during optic cup morphogenesis. *Biomech Model Mechanobiol* 15(6):1405–1421.
5. Shi Y, Yao J, Xu G, Taber LA (2014) Bending of the looping heart: Differential growth revisited. *J Biomech Eng* 136(8):0810021–08100215.
6. Milinkovitch MC, et al. (2013) Crocodile head scales are not developmental units but emerge from physical cracking. *Science* 339(6115):78–81.
7. Shyer AE, et al. (2013) Villification: How the gut gets its villi. *Science* 342(6155): 212–218.
8. Tallinen T, et al. (2016) On the growth and form of cortical convolutions. *Nat Phys* 12: 588–593.
9. Koyama H, et al. (2016) Mechanical regulation of three-dimensional epithelial fold pattern formation in the mouse oviduct. *Biophys J* 111(3):650–665.
10. Kleinman R, et al. (2008) *Walker's Pediatric Gastrointestinal Disease* (Decker, Hamilton, ON, Canada).
11. El-Gohary Y, Alagtal M, Gillick J (2010) Long-term complications following operative intervention for intestinal malrotation: A 10-year review. *Pediatr Surg Int* 26(2): 203–206.
12. Lee HC, Pickard SS, Sridhar S, Dutta S (2012) Intestinal malrotation and catastrophic volvulus in infancy. *J Emerg Med* 43(1):e49–e51.
13. Smith DM, Nielsen C, Tabin CJ, Roberts DJ (2000) Roles of BMP signaling and Nkx2.5 in patterning at the chick midgut-foregut boundary. *Development* 127(17):3671–3681.
14. Lyons KM, Hogan BL, Robertson EJ (1995) Colocalization of BMP 7 and BMP 2 RNAs suggests that these factors cooperatively mediate tissue interactions during murine development. *Mech Dev* 50(1):71–83.
15. Walton KD, et al. (2016) Villification in the mouse: Bmp signals control intestinal villus patterning. *Development* 143(3):427–436.
16. Arraf AA, Yelin R, Reshef I, Kispert A, Schultheiss TM (2016) Establishment of the visceral embryonic midline is a dynamic process that requires bilaterally symmetric BMP signaling. *Dev Cell* 37(6):571–580.
17. Sukegawa A, et al. (2000) The concentric structure of the developing gut is regulated by Sonic hedgehog derived from endodermal epithelium. *Development* 127(9): 1971–1980.
18. Roberts DJ, Smith DM, Goff DJ, Tabin CJ (1998) Epithelial-mesenchymal signaling during the regionalization of the chick gut. *Development* 125(15):2791–2801.
19. Shah RR, Nerurkar NL, Wang CC, Galloway JL (2015) Tensile properties of craniofacial tendons in the mature and aged zebrafish. *J Orthop Res* 33(6):867–873.
20. Fung Y-C (1993) *Biomechanics* (Springer, New York).
21. Sun J, et al. (2007) Deficient Alk3-mediated BMP signaling causes prenatal omphalocele-like defect. *Biochem Biophys Res Commun* 360(1):238–243.
22. Madison BB, et al. (2005) Epithelial hedgehog signals pattern the intestinal cryptvillus axis. *Development* 132(2):279–289.
23. Shyer AE, Huycke TR, Lee C, Mahadevan L, Tabin CJ (2015) Bending gradients: How the intestinal stem cell gets its home. *Cell* 161(3):569–580.
24. Pan Y, Heemskerk I, Ibar C, Shraiman BI, Irvine KD (2016) Differential growth triggers mechanical feedback that elevates Hippo signaling. *Proc Natl Acad Sci USA* 113(45): E6974–E6983.
25. Sutcliffe MC, Davidson JM (1990) Effect of static stretching on elastin production by porcine aortic smooth muscle cells. *Matrix* 10(3):148–153.
26. Shwartz Y, Blitz E, Zelzer E (2013) One load to rule them all: Mechanical control of the musculoskeletal system in development and aging. *Differentiation* 86(3):104–111.
27. Campinho P, et al. (2013) Tension-oriented cell divisions limit anisotropic tissue tension in epithelial spreading during zebrafish epiboly. *Nat Cell Biol* 15(12):1405–1414.
28. Legoff L, Rouault H, Lecuit T (2013) A global pattern of mechanical stress polarizes cell divisions and cell shape in the growing *Drosophila* wing disc. *Development* 140(19): 4051–4059.
29. Pouille P-A, Ahmadi P, Brunet A-C, Farge E (2009) Mechanical signals trigger Myosin II redistribution and mesoderm invagination in *Drosophila* embryos. *Sci Signal* 2(66): ra16.
30. Desprat N, Supatto W, Pouille PA, Beaurepaire E, Farge E (2008) Tissue deformation modulates twist expression to determine anterior midgut differentiation in *Drosophila* embryos. *Dev Cell* 15(3):470–477.
31. Collinet C, Rauzi M, Lenne P, Lecuit T (2015) Local and tissue-scale forces drive oriented junction growth during tissue extension. *Nat Cell Biol* 17(10):1247–1258.
32. Lecuit T, Lenne P-F (2007) Cell surface mechanics and the control of cell shape, tissue patterns and morphogenesis. *Nat Rev Mol Cell Biol* 8(8):633–644.
33. Weber GF, Bjerke MA, DeSimone DW (2012) A mechanoresponsive cadherin-keratin complex directs polarized protrusive behavior and collective cell migration. *Dev Cell* 22(1):104–115.
34. Csiszar A, et al. (2005) Regulation of bone morphogenetic protein-2 expression in endothelial cells: Role of nuclear factor-kappaB activation by tumor necrosis factor-alpha, H_2O_2, and high intravascular pressure. *Circulation* 111(18):2364–2372.
35. Sato M, et al. (1999) Mechanical tension-stress induces expression of bone morphogenetic protein (BMP)-2 and BMP-4, but not BMP-6, BMP-7, and GDF-5 mRNA, during distraction osteogenesis. *J Bone Miner Res* 14(7):1084–1095.
36. Sumanasinghe RD, Bernacki SH, Loboa EG (2006) Osteogenic differentiation of human mesenchymal stem cells in collagen matrices: Effect of uniaxial cyclic tensile strain on bone morphogenetic protein (BMP-2) mRNA expression. *Tissue Eng* 12(12): 3459–3465.
37. Cervantes S, Yamaguchi TP, Hebrok M (2009) Wnt5a is essential for intestinal elongation in mice. *Dev Biol* 326(2):285–294.
38. Geske MJ, Zhang X, Patel KK, Ornitz DM, Stappenbeck TS (2008) Fgf9 signaling regulates small intestinal elongation and mesenchymal development. *Development* 135(17):2959–2968.
39. Kan A, et al. (2013) SOX11 contributes to the regulation of GDF5 in joint maintenance. *BMC Dev Biol* 13(1):4.
40. Abzhanov A, Protas M, Grant BR, Grant PR, Tabin CJ (2004) Bmp4 and morphological variation of beaks in Darwin's finches. *Science* 305(5689):1462–1465.
41. Abzhanov A, Rodda SJ, McMahon AP, Tabin CJ (2007) Regulation of skeletogenic differentiation in cranial dermal bone. *Development* 134(17):3133–3144.
42. Logan M, Tabin C (1998) Targeted gene misexpression in chick limb buds using avian replication-competent retroviruses. *Methods* 14(4):407–420.
43. Murtaugh LC, Chyung JH, Lassar AB (1999) Sonic hedgehog promotes somitic chondrogenesis by altering the cellular response to BMP signaling. *Genes Dev* 13(2): 225–237.
44. Brent AE, Schweitzer R, Tabin CJ (2003) A somitic compartment of tendon progenitors. *Cell* 113(2):235–248.
45. Howard J (2001) *Mechanism of Motor Proteins and the Cytoskeleton* (Sinauer Associates, Sunderland, MA).

Supporting Information

Nerurkar et al. 10.1073/pnas.1700307114

SI Materials and Methods

Embryos and RCAS Infection. Fertilized White Leghorn chicken eggs (Charles River) and zebra finch eggs (kindly provided by Dr. Tim Gardner at Boston University, Boston, MA) were incubated at 38 °C to the desired stage. RCAS-BP (A) viral plasmid containing GFP (39), chick *Noggin* (40), and mouse *Bmp2* (41) cDNA were used to generate concentrated viral supernatant as described previously (39, 42). For infection of the embryonic chick gut and dorsal mesentery, 3–5 mL of albumin were removed from eggs at E3, before RCAS injection at E5. Infections were performed by injecting ∼200 nL of concentrated viral supernatant (with 0.01% Fast Green) through pulled capillary needles using a Picopump microinjector (World Precision Instruments). Infections were performed by injecting through the ventrolateral body wall at the level of the yolk stalk, targeting the coelomic space surrounding the midgut. Successful injection of this space was confirmed by spread of the Fast Green, which by exclusion makes the gut tube visible as a white tubular structure, and also leaks into the yolk stalk itself. On occasion, the needle tip pierced into the gut lumen, and in these cases the embryo was discarded. Following injection, windowed eggs were sealed with tape and incubated to the desired stage (42).

Section Immunofluorescence and in Situ Hybridization. Gut tissue was fixed overnight in 4% (wt/vol) paraformaldehyde (PFA) at 4 °C, rinsed with PBS, and then incubated 1 h at room temperature in 10% (wt/vol) sucrose and an additional 1 h in 20% (wt/vol) sucrose before an additional overnight incubation in 30% (wt/vol) sucrose at 4 °C. Samples were then frozen in OCT and cryosectioned to 16 μm. Sections within the distal jejunum and proximal ileum were used for further analysis; no proximo-distal variations were observed within this region. Staining was performed using the following primary antibodies: phospho-Smad 1/5/8 (1:300; 9511; Cell Signaling Technology), 3C2 (1:100; AMV-3C2; Developmental Studies Hybridoma Bank), Cy3-conjugated alpha smooth muscle actin (1:1,000; C6198; Sigma), and elastin (1:100; MAB2503; Millipore). With the exception of phospho-Smad, all primary antibodies were detected with fluorescently conjugated secondary antibodies (1:500). For phospho-Smad, samples were incubated with biotinylated secondary (1:500; 111 065 003; Jackson Immuno), followed by streptavidin HRP (1:500; 016 030 084; Jackson Immuno), and then visualized by tyramide amplification with TSA Plus Cy3 (1:100; 744001KT; Perkin-Elmer). Actin was visualized with Alexa Fluor 568-conjugated phalloidin (1:100; Thermo Fisher Scientific) in whole-mount dorsal mesentery that was fixed overnight at 4 °C in 4% (wt/vol) PFA following removal of the attached gut tube. All samples were counterstained with DAPI, mounted in Prolong Gold Antifade reagent (P36930; Thermo Fisher), and imaged on an inverted LSM 710 confocal microscope (Zeiss). In situ hybridization was performed using established methods (43, 44). For all immunofluorescent and in situ hybridization experiments, a minimum of three embryos was used.

Gut Morphometric Measurements. Small intestines were dissected from chicken embryos, and the superior mesenteric artery was dissected away to reveal the periodic structure of intestinal loops. From these, loop number and radius of curvature (R) were measured as described previously (1). Briefly, loop number was taken as the number of times the undulating gut crosses the antero-posterior axis, and R was measured from bright-field whole-mount images in ImageJ, using a circular path to fit the perimeter of each loop. The dorsal mesentery was then carefully separated from the gut tube. Bright-field images of each were taken, and length of the gut tube (L_t) and mesentery (L_m) was measured along their shared edge in ImageJ; the anterior and posterior boundaries for length measurement were taken as the end of the duodenal loop, and the proximal extent of the cecal horns, respectively. Wavelength λ was calculated as gut length divided by number of loops. The physiological growth strain ε_p, which quantifies stretching of the mesentery due to elongation of the attached gut tube, was calculated as $\varepsilon_p = L_t/L_m - 1$. Inner and outer gut radius (r_i and r_o, respectively) were measured from bright-field images of freshly dissected gut segments. Mesentery thickness (h) was measured by incubating freshly dissected mesentery tissue in Hoechst nuclear dye (1:500 in PBS; 33342; Thermo Fisher) at room temperature for 20 min, then imaging on a Zeiss LSM 710 confocal microscope to determine stack thickness through the tissue. Cell density was measured in whole-mount mesentery tissue stained with DAPI following dissection to remove the attached gut tube. For these, confocal stacks were collected, ∼0.1 mm^3 in volume, and cells were counted manually from z projections. Gut tube volume was calculated from mean values of tube radii and length as $V = \pi(r_o^2 - r_i^2)L_t$. Mesentery volume was computed from measuring surface area of the mesentery following removal of the gut tube, multiplied by the mean mesentery thickness h.

Uniaxial Tensile Testing. Uniaxial tensile testing of chick gut tube and mesentery was performed on dissected segments using a fine tungsten cantilever (127-μm diameter) as a force transducer (7, 19). Briefly, the free end of the tungsten cantilever was bent into a hook and used to pull on the tissue, while the fixed end was clamped to a fixture consisting of three manual, orthogonally arranged micrometer stages and a fourth stage driven by a linear actuator (Connex; Newport Corporation). As the base of the cantilever is displaced away from the sample, its opposing end pulls on the attached tissue sample. As the sample is stretched, the cantilever bends, and the associated force was calculated from deflection of the cantilever using the bending stiffness, given by the following (45):

$$k_b = \frac{3E\pi r^4}{4L^3},$$

where k_b is the bending stiffness, E = 410 GPa is the Young's modulus of tungsten, r = 0.064 mm is the cantilever radius, and the cantilever length L = 23 mm for gut tube and L = 17 mm for dorsal mesentery. A shorter length was used to accommodate larger magnitudes of force encountered during mesentery testing (k_b = 3.8 mN/mm, compared with 1.5 mN/mm for the gut tube). Deflection of the cantilever (δ) was calculated by tracking the tip displacement and subtracting from base displacement, calculated from the applied displacement rate. At the beginning and end of testing, empty tests were run (displacement with no deflection) to eliminate the possibility of hysteresis within the actuator. To apply forces to segments of gut tube, the two free ends were glued to a glass slide in a narrow U shape, and the free end of the tungsten cantilever was hooked through the center (Fig. S3*A*). A high-viscosity cyanoacrylate glue (Super Thick Cyanoacrylate Reef Glue; Crystal Clear Aquatics) wasused and applied to the fixed ends of the gut tube using a needle tip; due to autofluorescence of the glue, we directly confirmed that glue did not transfer beyond the anchoring points at the end of the gut tube. Glue was allowed ∼10 min to dry, during which time a thin plastic coverslip was placed over the gut tube to prevent drying. Spots of fluorescent vital dye DiO were injected onto the gut surface to serve as fiducial markers for strain measurement. Linear strain was calculated from two DiO

labels along the length of the tube as $\varepsilon = (l - l_o)/l_o$, where l is the deformed distance between the selected labels, and l_o is the distance between them at the start of testing. Force was applied by displacing the cantilever by a rate of 0.1% of gut length per second. Stress was calculated as $\sigma = k_b\delta/2\pi(r_o^2 - r_i^2)$, where δ is deflection of the tungsten cantilever, $r_{i/o}$ were measured from bright-field images of a neighboring segment of gut tube to the one tested, and the 2 in the denominator accounts for force being applied across two parallel arms of the U (strain was measured from only one arm; Fig. S3*A*). Due to a slight curvature of the gut tube, applying tension first results in unbending, and then stretching. Previously, we have shown that, for the wild-type gut tube, bending and extensional deformations give similar estimates of bending stiffness (1). Here, we confirmed that this is also true following misexpression of Bmp2 and Noggin.

For tensile testing of the dorsal mesentery, the intact small intestine was cut into strips using a vibratome (McIlwan Tissue Chopper), and segments of mesentery attached ~0.3–0.5 mm in width were isolated such that the gut tube was attached at one end, and the superior mesenteric artery at the other. The artery was pinned to a substrate of 5% agarose, and the free end of the tungsten cantilever was hooked through the lumen of the gut tube at the other end (Fig. S3*B*). The cantilever was then displaced at a constant rate of 0.01 mm/s, starting from a slacked position, and data were only collected once load began to increase continuously. Stress was calculated as $\sigma = k_b\delta/hw$, where w is the width of the sample and h is the mesentery thickness, measured from a neighboring piece of mesentery as described above. For both gut tube and mesentery testing, images were captured on a Leica stereoscope every 20 s, and FIJI was used to quantify displacements and δ by manual tracking. All tests were performed in PBS at room temperature on freshly dissected tissue. Modulus was calculated by fitting a linear regression to the linear region of the stress–strain curve; the transition strain ε^* was calculated as the x intercept of the regression (Fig. S3*C*).

Scaling Laws, Data Processing, and Statistics. As described previously, scaling laws arise from a static analysis of two structures—the gut tube and mesentery—that are bonded together under differential strain subsequent to differential elongation. All calculations and data processing, including scaling law predictions, were done in MATLAB. Statistical analyses were performed in GraphPad Prism. For comparisons across developmental stage (i.e., E8 vs. E12 vs. E16) and treatment (i.e., GFP vs. Bmp2 vs. Noggin), two-way ANOVAs were performed. For comparisons limited to a single stage, such as mechanical testing, which was performed only at E16, one-way ANOVAs were performed. For both two-way and one-way ANOVAs, statistical significance was determined using Tukey's post hoc test for $P \leq 0.05$.

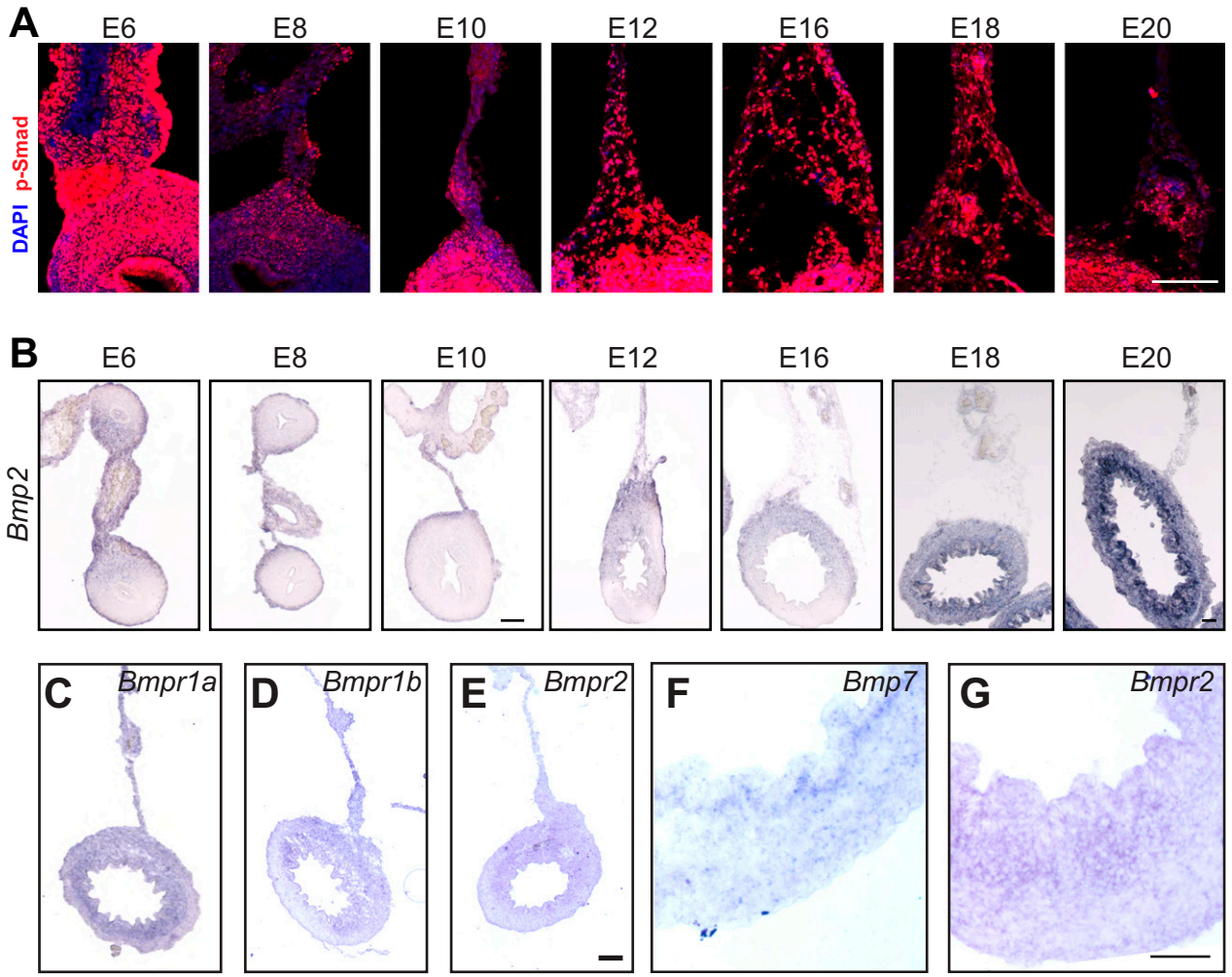

Fig. S1. Endogenous BMP activity in the gut and dorsal mesentery during looping. (*A*) Phospho-Smad staining of the dorsal mesentery from E6 through E20. (Scale bar: 100 μm.) (*B*) In situ hybridization for *bmp2* in the dorsal mesentery and gut tube from E6 through E20. [Scale bar (E6–E10) and (E12–E20): 100 μm.] (*C*–*E*) In situ hybridization for BMP type I receptors *Bmpr1a* (*C*) and *Bmpr1b* (*D*), type II receptor *Bmpr2* (*E*, magnified in *G*), and higher-magnification in situ hybridization of E12 ventral gut tube illustrating intense expression of BMP ligand *Bmp7* (*F*) and *Bmpr2* (*G*) in the mesenchyme adjacent to the endoderm. (Scale bar: 50 μm.) All sections are from the distal jejunum and proximal ileum.

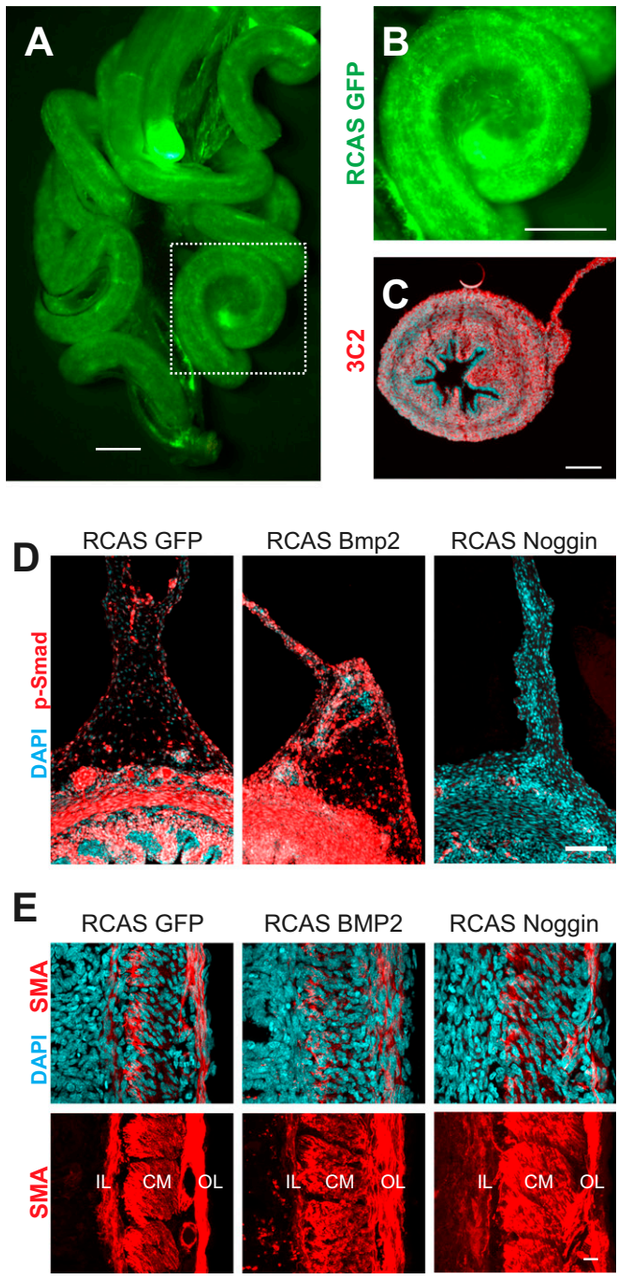

Fig. S2. Widespread RCAS infection of the gut permits modulation of BMP activity by RCAS-Bmp2 and RCAS-Noggin. (*A* and *B*) Fluorescent signal from RCAS-GFP–infected E16 small intestine demonstrates robust spread of the virus and misexpression of GFP throughout the gut tube and dorsal mesentery. Boxed region in *A* is magnified in *B*. (Scale bar: 1 mm.) (*C*) Immunofluorescent detection of RCAS viral coat protein 3C2 in section from RCAS-GFP–infected E12 gut, counterstained with DAPI. (Scale bar: 100 μm.) (*D*) Phospho-Smad 1/5/8 immunofluorescence in E16 chick intestines following infection with RCAS-GFP, RCAS-Bmp2, and RCAS-Noggin illustrates effective activation and inhibition of the BMP pathway. [Scale bar: 100 μm (*D*).] (*E*) Smooth muscle actin (SMA) immunofluorescence in E16 chick intestines following infection with RCAS-GFP, RCAS-Bmp2, and RCAS-Noggin illustrates that radial patterning of smooth muscle layers is unaltered. In addition, we observed no gross differences in attachment of the mesentery to the dorsal body wall, and no changes in loop morphology following dissection of the intestine from the embryo. This suggests that loop phenotypes were intrinsic to the tube and mesentery, and not imposed by changes in the interactions between the intestine and the surrounding embryonic tissues. Because looping and morphogenesis of the intestinal villi share a common physical mechanism, differential growth (7), and are regulated by the same pathway, BMP signaling (23), it is intriguing to consider whether morphogenesis of loops and villi may be somehow linked. Supporting this, Noggin misexpression, which resulted in a reduction of looping, did also result in the formation of large abnormal villus-like bulges in the endoderm (not shown). However, Bmp2 misexpression resulted in normal villi formation despite changes in looping. We therefore suspect that the villus phenotype in RCAS-Noggin–infected embryos was due to disruption of endogenous Bmp4 activity in the gut mesenchyme. Furthermore, villi emerge with no discernable dorsoventral heterogeneity, suggesting that this process is not significantly altered by curvature of the looped intestine. Related to this, we found that BMP inhibition by Noggin misexpression increased radial growth of the gut tube, whereas activation by Bmp2 misexpression had no effect. This, too, can likely be explained by the distinct, tissue-specific roles of different BMP ligands. Bmp4 expressed in the gut mesenchyme negatively regulates cell proliferation (23), and Noggin misexpression likely releases this growth control, leading to radial expansion of the tube. This effect was not restricted to the gut: a general increase in body size was observed as the virus spread throughout the embryo (Fig. S4). On the other hand, the reduction in growth of the mesentery following RCAS-Bmp2 infection appeared relatively tissue specific, as no changes in tube geometry or overall growth of the embryo were observed. (Scale bar: 10 μm.) CM, circumferential smooth muscle layer; IL, inner longitudinal smooth muscle layer; OL, outer longitudinal smooth muscle layer.

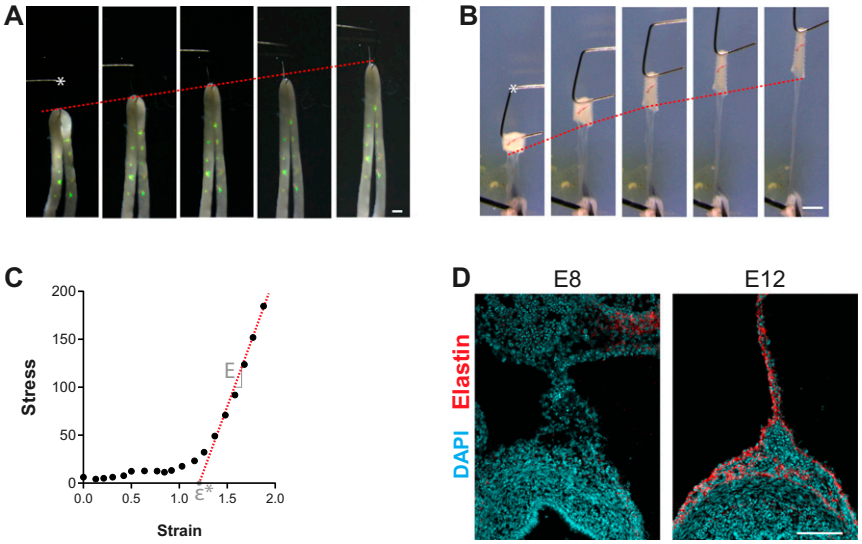

Fig. S3. Uniaxial tensile testing and elastin accumulation in the gut tube and mesentery. (*A* and *B*) For uniaxial tensile testing of gut tube (*A*) and mesentery (*B*), we developed a micromechanical tester that uses a fine tungsten cantilever (*) driven by a piezoelectric actuator to simultaneously apply and measure tensile forces on the order of approximately nanonewtons to micronewtons (7, 19). (Scale bar: 1 mm.) (*C*) Sample stress–strain curve indicating the modulus *E* as the slope of a line fit to the linear/constant-slope region of the curve (red dashed line), and the transition strain ε^*, determined as the intersection of this line with the *x* axis. (*D*) Immunofluorescent detection of elastin in the wild-type chick intestine at E8 (before looping) and E12 (midlooping). (Scale bar: 100 μm.)

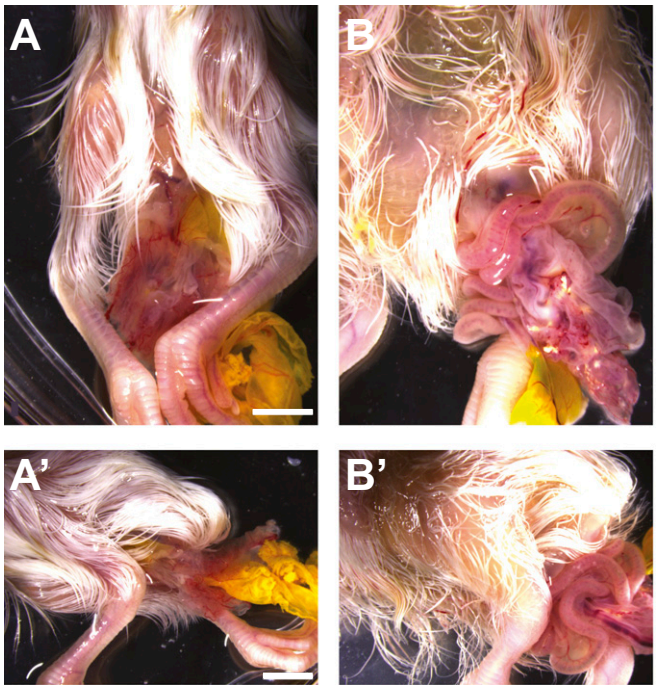

Fig. S4. BMP signaling required for internalization of the small intestine. Ventral (*A*) and latera (*A′*) views of E20 RCAS-GFP–infected chicken embryo with membranes of the yolk stalk extending from the embryo. Ventral (*B*) and lateral (*B′*) views of gastroschisis in E20 RCAS-Noggin–infected chicken embryo. Gastroschisis was observed in $n = 4/4$ RCAS-Noggin embryos, compared with $n = 0/4$ RCAS-GFP embryos. (Scale bar: 5 mm.)